6th European Conference on Computational Mechanics (ECCM 6)
7th European Conference on Computational Fluid Dynamics (ECFD 7)
1115 June 2018, Glasgow, UK

VARIATIONAL MODELING OF MICRO-CRACKING AND FAILURE IN FIBER-REINFORCED CONCRETES

G. LANCIONI[1] R. ALESSI[2] and E. BAIONI[3]

[1] Dipartimento di Ingegneria Civile, Edile e Architettura, Universita Politecnica delle Marche, Via Brecce Bianche, 60131 Ancona, Italy, g.lancioni@univpm.it

[2] Dipartimento di Ingegneria Strutturale e Geotecnica, Sapienza Universita di Roma, Piazzale Aldo Moro 5, 00185 Roma, Italy, roberto.alessi@uniroma1.it

[3] Computational Mechanics, Civil Research Group, School of Engineering, University of Warwick, Coventry CV4 7AL, UK, elisa_baioni@libero.it.

Key words: Phase-field theory, variational fracture, micro-cracking, fiber-reinforced concrete.

Abstract. A variational micro-mechanical model is proposed to reproduce the complex response of fiber-reinforced concretes to tensile loadings. The composite is described as a mixture where two phases are combined: a brittle phase, corresponding to the cementitious matrix, and an elasto-plastic phase, describing the ductile contribution of fibers. The model is formulated in the simple one-dimensional setting of a tensile bar, and implemented in a finite element code. Simulations of tensile tests are performed, which capture the different stages of the evolution typically observed in experiments: the stress-hardening phase of microcracking, and the subsequent stage of stress-softening in which a macro-crack opens, leading to the sample failure. Simulations also reproduce the stiffness degradation and the occurrence of residual strains observed when samples are unloaded.

1 INTRODUCTION

The mechanical properties of standard concrete significantly improve when fibers, made of steel or plastic, are distributed into the cementitious matrix. In particular, fibers contribute to sustain tensile loadings and to diffuse stresses, thus largely increasing the ultimate strength and ductility. Focusing on the tensile behavior, for which significant mechanical enhancements are achieved [1, 2, 3], High Performance Fiber Reinforced Concretes (HPFRC) typically experience an initial elastic strain phase, followed by a non-linear stress-hardening process of diffuse micro-cracking, and a final stress-softening stage, corresponding to strain localization and macro-crack opening. These three phases are clearly illustrated in Fig. 1.

A variational model was developed in [4] to reproduce the complex mechanical response of HPFRCs. By incorporating a damage parameter, it interprets micro-cracking as diffuse damaging, and macro-crack opening as damage localization. Instead, in this work, a variational micro-mechanical model is proposed where the mechanics of cementitious matrix and fibers is described by two material phases accounting for brittle and ductile elasto-plastic responses. In addition to the elastic strain energy, which is assumed to be quadratic with respect to the elastic strain, as in linear elasticity, specific energies are assigned to the two materials: *i.* damage energy is assigned to the brittle material, which depends on a scalar damage parameter, and accounts for a local and a non-local contribution that are typically considered in phase-field models of fracture [5]; *ii.* a plastic energy is considered for the ductile phase, which is similar to that proposed in [6, 7, 8]. It is sum of a local non-convex energy, which has a dissipative nature, and a non-local term, depending on the plastic strain gradient.

Damage and plasticity are considered separately within each component of the mixture, differently than [9, 10], where damage and plasticity are combined within the same material. The two phases are linked through linear elastic diffuse interface, which contributes to couple the problems of each phases. The structure of the resulting formulation is similar to that proposed in [11] for the failure study of hybrid laminates. The evolution problem is formulated as an incremental energy minimum problem, where the unknowns are the rates of displacements and internal variables (damage and plastic strain fields) associated to the two phases.

The proposed model is capable to reproduce the progressive formation of micro-cracks within the brittle material phase representing the cementitious matrix, as observed in experiments, thus providing a more realistic description of the micro-cracking process than the model in [4]. The macro-crack growth, which concludes the deformation process, is described by progressive plastic strain localization in the ductile material. The model also improves the description of the unloading process, since it accounts for stiffness degradation, which produces a reduction of the slope of the unloading stress-strain curve, and plastic dissipation, which introduces residual strains, according to the experimental evidences (see the unloading branch of Fig. 1).

In the present paper, the model is formulated in the simple one-dimensional setting of a tensile bar, and it is numerically implemented in a finite element code. Numerical simulations are performed and results are discussed, highlighting the predictive abilities of the model in capturing the main feature of the evolution process observed in tensile tests.

The paper is organized as follows. In Sect. 2, the basic experimental evidences of tensile tests on HPFRC samples are presented. The model is formulated in Sect. 3 and numerical results are discussed in Sect. 4. Conclusions and perspectives for future researches are drawn in Sect. 5.

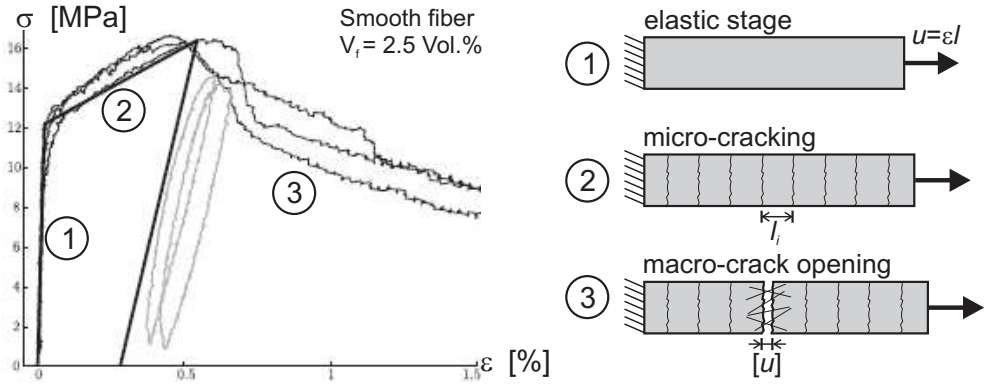

Figure 1: Experimental stress-strain curve of tensile tests on dog-bone shaped samples (from [2]).

2 TENSILE RESPONSE OF FIBER-REINFORCED CONCRETE

To give an insight into the enhanced mechanical performances of HPFRC, typical stress-strain curves obtained from tensile tests on dog-bone specimens are drawn in Fig. 1. They are taken from [2], where several experiments are performed, considering different types of fibers and different fiber volume fractions. The curves of Fig. 1 result from tests on samples reinforced with straight fibers of 13 mm in length, and volume fraction equal to 2.5 Vol.%.

Each curve exhibits three different peculiar branches, labeled by different numbers, which are associated to different stages of evolution. First, the sample stretches elastically, corresponding to the initial straight stress-strain curve 1, which terminates when the stress reaches the limit value of about 12 MPa. From this point on, the bar experiences a process of micro-cracking, where multiple cracks progressively forms in the cementitious matrix, almost uniformly distributed through the bar. For the tests represented in Fig. 1, the crack width ranges between 5 and 20 μm, and crack spacing is about 4.2 mm. This multi-cracking phase occurs in regime of stress-hardening, and corresponds to the increasing sawtooth branch of the stress-strain curve 2. Stress drops correspond to micro-cracks opening. It is worth noting that such a hardening stage, totally absent in common concretes, is due to the bridging effect of the fibers across the micro-cracks. Moreover, such a bridging effect is the key mechanism that significantly enhance the material ductility. The stress-softening stage 3 concludes the evolution process leading to the sample failure. More precisely, during the softening stage, the weakest micro-crack evolves into a macro-crack, where the bridging fibers progressively pull out and break, whereas the remaining micro-cracks elastically unload without the occurrence of further matrix cracks.

Unloading branches are plotted in Fig. 1 as well. They have smaller slope than the initial elastic curve and unveils the presence of residual strains. The smaller slope testifies a stiffness degradation related to the formation of micro-cracks in the cementitious matrix whereas residual strains are related to the evolution of plasticity both during the hardening and softening stages.

3 VARIATIONAL MODEL

In this section, the variational model is presented in the simple one-dimensional setting. A bar of length l is considered, subjected to the stretching displacement $\varepsilon(t)l$ (with ε the assigned strain and t a time-like evolution parameter). Positions in the longitudinal axis are referred with $x \in (0, l)$. A geometrical scheme of the problem is drawn in Fig. 2. The bar is a mixture of two phases, a brittle phase (phase 1) and a ductile plastic phase (phase 2), which represent the cementitious matrix and fibers (combined with large aggregates), respectively. The volume fractions per unit length of the two phases are v_1 and $v_2 = 1 - v_1$. The area per unit length of the interface between the two phases is a.

In the following, indices 1 and 2 are used to refer to phase 1 and 2. Furthermore, when necessary, a subscript t is used to indicate dependence on the time evolution parameter t, called from now on simply *time* for brevity. With regard to derivatives, a prime and a dot indicate derivatives with respect to x and t, respectively, i.e., given a function $v = v_t(x)$, $v' = dv/dx$, and $\dot{v} = dv/dt$.

3.1 Modeling assumptions

Here, the basic modeling assumptions are stated. The state variables are the displacements $u_1(x)$ and $u_2(x)$ of the two phases, the damage variable $\alpha(x)$ defined in phase 1, and the plastic strain $p(x)$ defined in phase 2. The damage variable α ranges between 0 and 1: $\alpha = 0$ means sound material, and $\alpha = 1$ means fully damaged material, *i.e.* a crack. The irreversibility condition

$$\dot{\alpha} \geq 0 \tag{1}$$

is imposed in order to prevent material self-healing.

The internal energy of the bar is

$$\begin{aligned} \mathcal{E}(u_1, u_2, \alpha, p) = & \int_0^l v_1 \left(\frac{1}{2}(1-\alpha)^2 E_1 u_1'^2 + w_1 \alpha + \frac{1}{2} w_1 l_1^2 \alpha'^2 \right) dx + \\ & + \int_0^l v_2 \left(\frac{1}{2} E_2 (u_2' - p)^2 + w_2(p) + \frac{1}{2} A l_2^2 p'^2 \right) dx + \\ & + \int_0^l a \frac{1}{2} k_a (u_1 - u_2)^2 \, dx. \end{aligned} \tag{2}$$

The first integral represents the internal energy of phase 1. Its expression originates from standard phase-field models, where the damage energy $w_1\alpha$ is a linear function of α in order to account for an initial elastic stage (see [12]). The second integral is the internal energy of phase 2, which is analogous to the energies considered in the nonlocal plasticity models of [6, 7]. The plastic energy $w_2(p)$ is a strictly increasing function, such that $w_2(0) = 0$ and $w_2'(0) > 0$. Moreover, we suppose that w_2 is totally dissipated, that is

$$\dot{w}_2(p) = w_2'(p)\dot{p} \geq 0, \tag{3}$$

which, since $w_2'(p) > 0$, reduces to

$$\dot{p} \geq 0. \tag{4}$$

In classical gradient plasticity [13], the plastic energy depends on the cumulated plastic strain, which, in the one-dimensional tensile contest considered here, coincides with the irreversible plastic strain p. Parameters l_1 and l_2 are internal lengths of phases 1 and 2, aiming at governing the respective localization widths. Finally, the third integral in (2) is the linear elastic interface energy as a function of the relative displacements linking the two phases.

According to the scheme of Fig. 2, the boundary conditions are

$$\begin{array}{l} u_1(0) = u_2(0) = 0, \quad u_1(l) = u_2(l) = \varepsilon(t) l, \\ \alpha(0) = \alpha(l) = 0, \quad p(0) = p(l) = 0. \end{array} \tag{5}$$

Damage and plastic strain are assigned null at the boundaries in order to keep inelastic phenomena away from the bar endpoints, and, thus, to reproduce results usually observed in experiments. Indeed, in the tensile tests described in Sect. 2, specimens are enlarged at the end sections (bone-shaped samples) to avoid inelastic phenomena, and eventually premature failure at the gripping regions.

Stresses in the two phases, and the interface shear stress are

$$\sigma_1 = (1-\alpha)^2 E_1 u_1', \quad \sigma_2 = E_2(u_2' - p), \quad \tau_a = k_a(u_1 - u_2), \tag{6}$$

and they are obtained by derivation of the internal energy densities and interface energy in (2) with respect to the observable variables u_1', u_2' and the slip $u_1 - u_2$.

3.2 Equilibrium

Equilibrium equations are obtained by requiring that the energy first variation

$$\begin{aligned} \delta\mathcal{E}(u_1, u_2, \alpha, p)[z_1, z_2, \beta, q] = & \int_0^l \left\{ \left(a\tau_a - v_1\sigma_1'\right) z_1 + \left(-(1-\alpha)E_1 u_1'^2 + w_1 - w_1 l_1^2 \alpha''\right)\beta \right\} dx + \\ & + \int_0^l \left\{ \left(-v_2\sigma_2' - a\tau_a\right) z_2 + \left(-\sigma_2 + w_2'(p) - A l_2^2 p''\right) q \right\} dx \\ & + \left[v_1 \left(\sigma_1 z_1 + w_1 l_1^2 \alpha' \beta\right) + v_2 \left(\sigma_2 z_2 + A l_2^2 p' q\right) \right]_0^l, \end{aligned} \tag{7}$$

be non-negative for any perturbation (z_1, z_2, β, q), such that $\beta \geq 0$ and $q \geq 0$. The resulting equations are:

$$\begin{array}{lll} v_1\sigma_1' - a\tau_a = 0, \quad v_2\sigma_2' + a\tau_a = 0, & & \text{balance equations,} \\ f_1(u_1, \alpha) = -(1-\alpha)E_1 u_1'^2 + w_1 - w_1 l_1^2 \alpha'' \geq 0, & & \text{damage yield condition,} \\ f_2(u_2, p) = w_2'(p) - A l_2^2 p'' - \sigma_2 \geq 0 & & \text{plastic yield condition.} \end{array} \tag{8}$$

By using $(6)_1$, inequality $(8)_3$ turns into

$$\sigma_1 \leq \sqrt{E_1(1-\alpha)^3(w_1 - w_1 l_1^2 \alpha'')} = \sigma_{y1}(\alpha), \tag{9}$$

with $\sigma_{y1}(\alpha)$ the damage yield stress. The limit elastic stress

$$\sigma_{e1} = \sigma_{y1}(0) = \sqrt{E_1 w_1}, \tag{10}$$

is the maximum stress that phase 1 can sustain before damaging. Analogously, $(8)_4$ rewrites

$$\sigma_2 \leq w_2'(p) - Al_2^2 p'' = \sigma_{y2}(p), \tag{11}$$

with σ_{y2} the plastic yield stress, and, in this case, the limit elastic stress is

$$\sigma_{e2} = \sigma_{y2}(0) = w_2'(0). \tag{12}$$

Boundary terms in (7) are null because of the boundary conditions (5).

3.3 Evolution

Time t is discretized into intervals of length τ, and, within each time step $t \mapsto t+\tau$, the evolution is governed by the incremental energy minimization problem described in the following.

At time $t+\tau$, the problem unknowns are approximated by the linear approximations

$$u_{j,t+\tau} = u_{j,t} + \tau \dot{u}_{j,t},\ j = 1,\, 2, \quad \alpha_{t+\tau} = \alpha_t + \tau\dot{\alpha}_t, \quad p_{t+\tau} = p_t + \tau \dot{p}_t, \tag{13}$$

and the energy (2) is developed up to the second order as follows

$$\begin{aligned}\mathcal{E}\left(u_{1,t+\tau}, u_{2,t+\tau}, \alpha_{t+\tau}, p_{t+\tau}\right) \simeq\ & \mathcal{E}\left(u_{1,t}, u_{2,t}, \alpha_t, p_t\right) + \tau\dot{\mathcal{E}}\left(u_{1,t}, u_{2,t}, \alpha_t, p_t, \dot{u}_{1,t}, \dot{u}_{2,t}, \dot{\alpha}_t, \dot{p}_t\right) + \\ & \frac{1}{2}\tau^2\ddot{\mathcal{E}}\left(u_{1,t}, u_{2,t}, \alpha_t, p_t, \dot{u}_{1,t}, \dot{u}_{2,t}, \dot{\alpha}_t, \dot{p}_t\right).\end{aligned} \tag{14}$$

We suppose that solution $(u_{1,t}, u_{2,t}, \alpha_t, p_t)$ at instant t is known, and we look for the unknown rates $(\dot{u}_{1,t}, \dot{u}_{1,t}, \dot{\alpha}_t, \dot{p}_t)$ that minimize (14) under the constraints (1) and (4), and with the boundary conditions

$$\dot{u}(0) = 0, \quad \dot{u}(l) = \dot{t}l \quad \dot{\alpha}(0) = \dot{\alpha}(l) = 0, \quad \dot{p}(0) = \dot{p}(l) = 0. \tag{15}$$

Solution at the instant $t+\tau$ is determine from the approximated expression (13). Since $\mathcal{E}\left(u_{1,t}, u_{2,t}, \alpha_t, p_t\right)$ is constant, (14) reduces to

$$\mathcal{J}\left(\dot{u}_{1,t}, \dot{u}_{2,t}, \dot{\alpha}_t, \dot{p}_t\right) = \dot{\mathcal{E}}\left(u_{1,t}, u_{2,t}, \alpha_t, p_t, \dot{u}_{1,t}, \dot{u}_{2,t}, \dot{\alpha}_t, \dot{p}_t\right) + \frac{1}{2}\tau\ddot{\mathcal{E}}\left(u_{1,t}, u_{2,t}, \alpha_t, p_t, \dot{u}_{1,t}, \dot{u}_{2,t}, \dot{\alpha}_t, \dot{p}_t\right), \tag{16}$$

where $\dot{\mathcal{E}}$ and $\ddot{\mathcal{E}}$ have the explicit expressions

$$\begin{aligned}\dot{\mathcal{E}} =& \int_0^l \{v_1(1-\alpha)^2 E_1 u_1' \dot{u}_1' + v_2 E_2 (u_2' - p)\dot{u}_2' + a\tau_a(\dot{u}_1 - \dot{u}_2) + \\ &+ v_1[(-(1-\alpha)E_1 u_1'^2 + w_1)\dot{\alpha} + w_1 l_1^2 \alpha' \dot{\alpha}'] + v_2[(-E_2(u_2' - p) + w_2'(p))\dot{p} + Al_2^2 p' \dot{p}']\}\, dx \\ \ddot{\mathcal{E}} =& \int_0^l \{v_1(1-\alpha)^2 E_1 \dot{u}_1'^2 + v_2 E_2 \dot{u}_2'^2 + ak_a(\dot{u}_1 - \dot{u}_2)^2 - 4v_1(1-\alpha)E_1 u_1' \dot{u}_1' \dot{\alpha} + \\ &- 2v_2 E_2 \dot{u}_2' \dot{p} + v_1(E_1 u_1'^2 \dot{\alpha} + w_1 l_1^2 \dot{\alpha}'^2) + v_2(E_2 \dot{p}^2 + w_2''(p)\dot{p}^2 + Al_2^2 \dot{p}'^2)\} dx,\end{aligned} \tag{17}$$

and the minimum problem writes

$$(\dot{u}_{1,t}, \dot{u}_{2,t}, \dot{\alpha}_t, \dot{p}_t) = \operatorname{argmin} \{\mathcal{J}(\dot{u}_1, \dot{u}_2, \dot{\alpha}, \dot{p}),\ \dot{\alpha} \geq 0,\ \dot{p} \geq 0,\ + \text{b.c.}\}\,. \tag{18}$$

Necessary condition for a minimum is that

$$\delta\mathcal{J}\,(\dot{u}_{1,t}, \dot{u}_{2,t}, \dot{\alpha}_t, \dot{p}_t)\,[\delta\dot{u}_1, \delta\dot{u}_2, \delta\dot{\alpha}, \delta\dot{p}] \geq 0, \tag{19}$$

for any $\delta\dot{u}_1$, $\delta\dot{u}_2$, $\delta\dot{\alpha}$ and $\delta\dot{p}$ which are null at the endpoints, and satisfy the constraints

$$\dot{\alpha}_t + \delta\dot{\alpha} \geq 0, \quad , \quad \dot{p}_t + \delta\dot{p} \geq 0, \tag{20}$$

which leads to the following evolution equations:
(i) stress balance equations

$$v_1\dot{\sigma}'_{1,t} - a\dot{\tau}_{a,t} = 0, \qquad v_2\dot{\sigma}'_{2,t} + a\dot{\tau}_{a,t} = 0, \tag{21}$$

(ii) damage Kuhn-Tucker relations

$$\dot{\alpha}_t \geq 0, \quad f_{1,t} + \tau\dot{f}_{1,t} \geq 0, \quad \dot{\alpha}_t(f_{1,t} + \tau\dot{f}_{1,t}) = 0, \tag{22}$$

(iii) plastic Kuhn-Tucker relations

$$\dot{p}_t \geq 0, \quad f_{2,t} + \tau\dot{f}_{2,t} \geq 0, \quad \dot{p}_t(f_{2,t} + \tau\dot{f}_{2,t}) = 0, \tag{23}$$

where f_1 and f_2 are defined in $(8)_{3,4}$. Relations (22) and (23) are consistency conditions that state that damage and plastic strain can increase only if the corresponding yield functions maintain equal to zero. A consequence of assumptions (13) and (14) is that the evolution problems (22) and (23) linearly depend on τ, and the accuracy of the evolution problem increases if smaller and smaller values of τ are assigned. In the numerical simulations, accuracy is improved by implementing a iterative minimization algorithm at each time step.

4 SIMULATIONS

At each time step, the minimum problem (18) is solved numerically by finite elements. An alternate minimization algorithm is implemented, which consists in minimizing the functional $\mathcal{J}$ with respect to each one of the variables $(\dot{u}_1, \dot{u}_2)$, $\dot{\alpha}$ and $\dot{p}$, keeping fixed all the others. The minimum problems with respect to $\dot{\alpha}$ and $\dot{p}$ are solved by using a constrained quadratic programming routine, in order to enforce the irreversibility conditions (1) and (4), whereas minimization with respect to $(\dot{u}_1, \dot{u}_2)$ results in a stationarity linear equation. Alternate minimization is iterated until convergence.

4.1 Parameters setting

Since we intend to reproduce the experimental response of Fig. 1 taken from [2], values of many parameters of the model are fixed equal to those indicated in [2]. The parameters

which do not have corresponding experimental values are fixed in order to get the best curve fitting. The problem geometry is schematized in Fig. 2(a), where the length $l = 76$ mm is that of the samples tested in [2]. We assign $v_1 = 0.965$, $v_2 = 0.035$ and $a = 1$. For the Young's moduli, we assume $E_1 = 56\,\text{GPa}$ and $E_2 = 210\,\text{GPa}$. The damage coefficient w_1 is determined from (10), by assigning $\sigma_{e1} = 11$ MPa. A small perturbation has been introduced in the values of σ_{e1} in order to recreate the heterogeneity always present in real materials. The internal length l_1 is related to the width of the process zone h_1, here chosen as $h_1 = 0.1\,\text{mm}$, by the relation $l_1 = h_1/(2\sqrt{2})$ deduced in [12]. The tentative value $k_a = 4000\ \text{N/mm}^2$ is assigned to the interface elastic coefficient. The plastic energy $w_2(p)$ is chosen as simple as possible. A tentative quadratic convex-concave function is assumed, whose graph is plotted in Fig. 2(b). Notice that $w_2'(0)$ is the plastic yield value σ_{e2}, according to formula (12), which is assumed equal to 55 MPa. The nonlocal coefficient of the plastic energy is $Al_2^2 = 3.8\ \text{N mm}^2$.

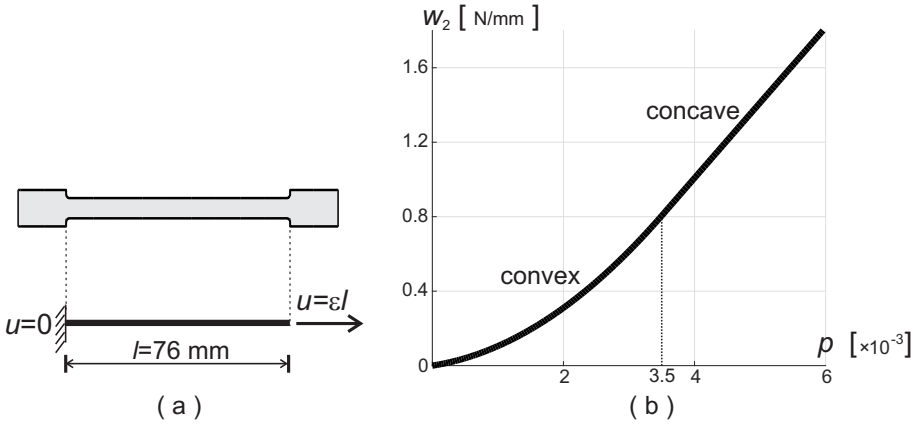

Figure 2: (a) Geometrical scheme of the bar. (b) Plastic energy graph.

4.2 Numerical results

The resulting numerical stress-strain curve is plotted in Fig. 3. The very same three branches of the experimental curve of Fig. 1 are observed, which are the initial linearly elastic curve, the sawtooth branch associated to the stress hardening micro-cracking evolution, and the final softening branch associated to a macro-crack opening. Each drop of the stress-hardening curve corresponds to the opening of 1 micro-crack (2 contemporary micro-cracks for the deepest drops). Curve jumps are deeper than those of the experimental curves of Fig. 1 since, in the proposed one-dimensional formulation, each crack opens through the whole cross-section of the sample, while many cracks of small area form in in real samples. As a result, the experimental response curves present more drops of smaller amplitude.

The progressive formation of micro-cracks is described in Fig. 4. White lines are used to show the position of matrix (phase 1) cracks within the bar at different values of ε. The distribution of cracks is quite periodic through the bar, with increasing frequency

during the evolution. New cracks open in between adjacent preexisting cracks that have the largest spacing.

Fig. 5 illustrates the mechanism of crack opening in terms of stresses. In it, profiles of σ_1 and σ_2 are drawn at different values of ε in the evolution stages of second crack opening (Fig. 5a) and tenth and eleventh cracks opening (Fig. 5b). At crack points, σ_1 is null, and σ_2 attains the maximum value. The bell-shaped profiles of σ_1 in between adjacent cracks growth as ε increases, and, when the midpoint of one bell (the largest one) reaches the limit value σ_{e1} of formula (10), represented by the red line in Fig. 5, a new crack forms therein. The stress σ_1 jumps to zero in correspondence of the new crack, and it globally reduces in the whole bar, as shown by the blue profiles.

Profiles of u_1, u_2 and p at different values of ε are drawn in Fig. 6. While u_1 tends to be discontinuous at cracks points, u_2 remains smoother (continuous). Indeed, the elasto-plastic phase 2 does not break, but it undergoes plastic strains in small zones crossing the cracks (see the profiles of p in Fig. 6). Fig. 6d draws a picture of what happens in the softening regime: plastic strain localizes and considerably grows in a small region in the middle of the bar. This leads to a large jump of displacements u_1 and u_2, which reproduces macro-crack opening. In the zone where macro-crack evolves, the plastic strain attains values larger than $p = 0.35$ %, thus belonging to the concave branch of the plastic energy of Fig. 2b.

Finally, we notice that the model also gives an accurate description of the unloading process, which is purely elastic. The unloading curve of Fig. 3 is very similar to the experimental curve of Fig. 1, capturing both stiffness degradation due to micro-cracking, and residual plastic strains, because of the dissipative nature of the plastic energy of phase 2.

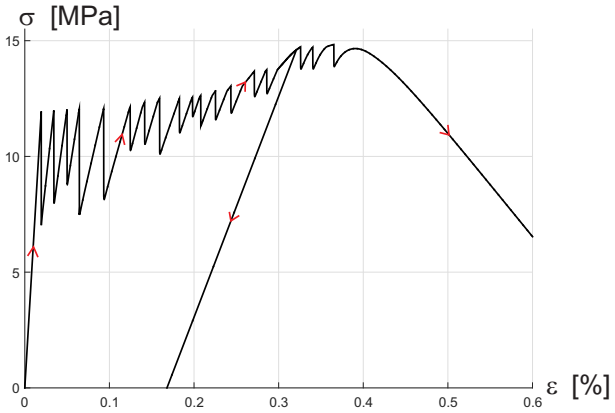

Figure 3: Numerical σ-ε curve.

5 CONCLUSIONS

A variational bi-phase model has been presented aimed at describing the rich mechanical response of high-performance fiber-reinforced concretes subjected to tensile loadings. The model accounts for a mixture of a brittle phase and an elasto-plastic phase, which

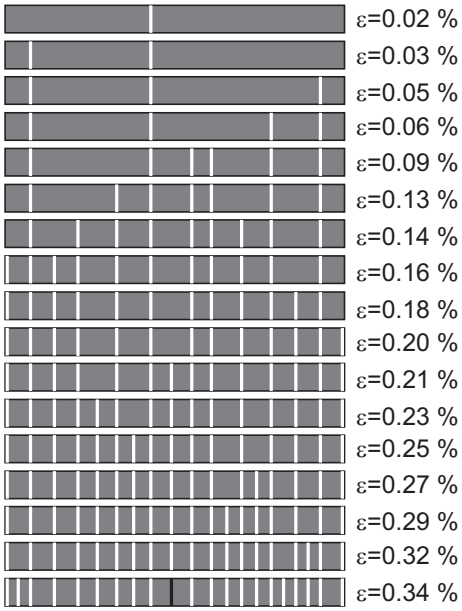

Figure 4: Sequence of microcrack openings for increasing ε. The black crack at $\varepsilon = 0.34\,\%$ is the macro-crack that leads to the bar failure.

represent the cementitious matrix and the fibers, respectively. The formulation has been conducted in the simple one dimensional case of a tensile bar, and equilibrium and evolution laws have been variationally deduced and numerically implemented. Numerical simulations have shown the ability of the model in capturing the peculiar features of the tensile failure processes observed in experiments, such as micro-cracking, ductile macro-crack opening, elastic unloading, stiffness degradation, plastic strains accumulation.

The study is open to many developments, which will be addressed in future researches. We point out three lines of research, which are already object of study: *1.* extension of the model to multi-dimensional frameworks; *2.* application of the model to the design of real objects made of HPFRC, as in [14], where a table prototype totally made of HPFRC was studied; *3.* analysis of the effects of heterogeneous distribution of fibers within the cementitious matrix on the mechanical performances.

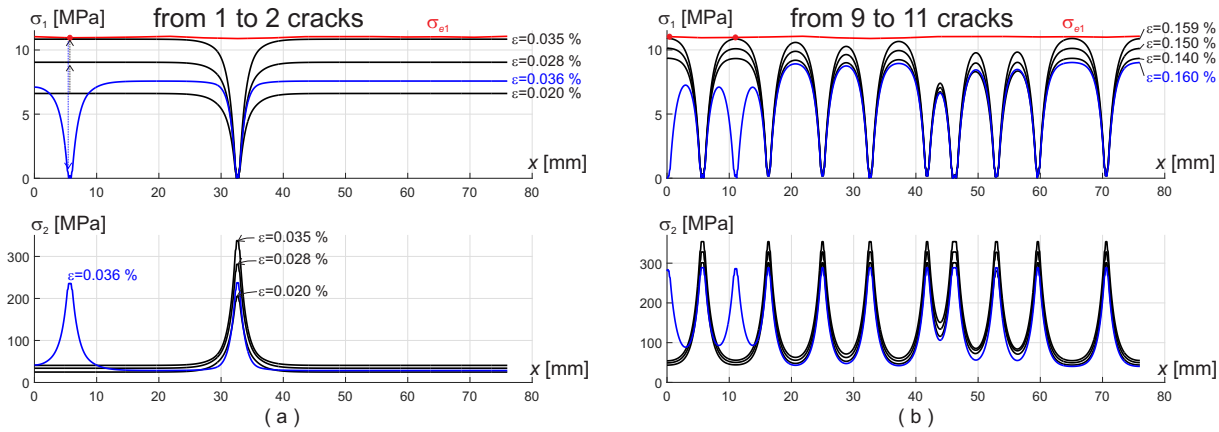

Figure 5: Profiles of stresses σ_1 and σ_2 at different values of ε in the evolution stages from 1 to 2 cracks (a), and from 9 to 11 cracks (b)

REFERENCES

[1] S.H. Park, D.J. Kim, G.S. Ryu, K.T. Koh, Tensile behavior of Ultra High Performance Hybrid Fiber Reinforced Concrete, *Cement and Concrete Composites*, Vol. **34**, pp. 172–184, 2012.

[2] K. Wille, S. El-Tawil, A.E. Naaman, Properties of strain hardening ultra high performance fiber reinforced concrete (UHP-FRC) under direct tensile loading. *Cement and Concrete Composites*, Vol. **48**, pp. 53–66, 2014.

[3] P. Maca, R. Sovjak, T. Vavrinik, Experimental Investigation of Mechanical Properties of UHPFRC, *Procedia Engineering*, Vol. **65**, pp. 14–19, 2013.

[4] G. Lancioni, V. Corinaldesi, Variational modelling of diffused and localized damage with applications to fiber-reinforced concretes. *Meccanica*, Vol. **53**, pp. 531–551, 2017.

[5] J.-J. Marigo, C. Maurini, and K. Pham. An overview of the modelling of fracture by gradient damage models. *Meccanica*, **51**(12), pp. 3107–3128, 2016.

[6] G. Del Piero, G. Lancioni, R. March, A diffuse cohesive energy approach to fracture and plasticity: the one-dimensional case. *Journal of Mechanics of Materials and Structures*, Vol. **8**(2-4), pp. 109–151, 2013.

[7] L. Lancioni, Modeling the Response of Tensile Steel Bars by Means of Incremental Energy Minimization. *Journal of Elasticity*, Vol. **121**, pp. 25–54, 2015.

[8] G. Lancioni, T. Yalcinkaya, A. Cocks, Energy based non-local plasticity models for deformation patterning, localization and fracture. *Proceedings of the Royal Society A*, Vol. **471**: 20150275, pp. 1–23, 2015.

[9] R. Alessi, J.J. Marigo, S. Vidoli, Gradient damage models coupled with plasticity: Variational formulation and main properties, *Mechanics of Materials*, Vol. **80**(B), pp. 351–367, 2015.

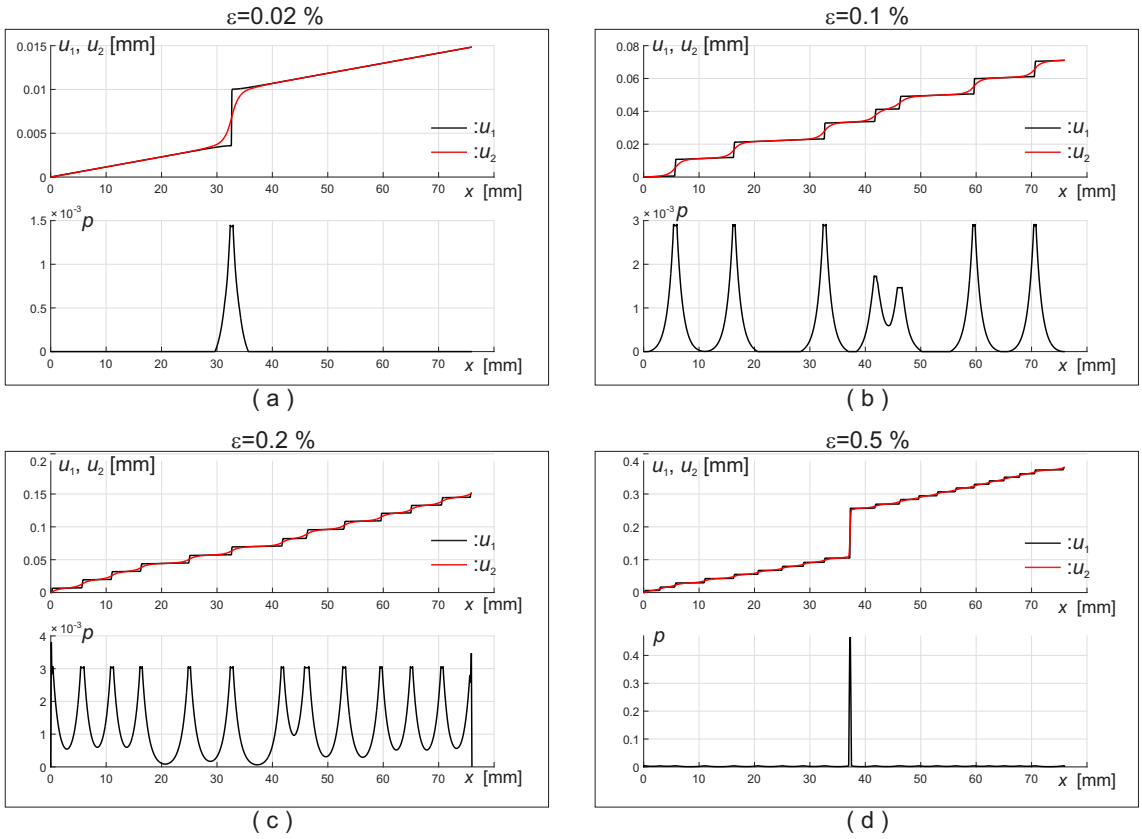

Figure 6: Profiles of u_1, u_2 and p at different values of ε

[10] R. Alessi, J.J. Marigo, C. Maurini, S. Vidoli, Coupling damage and plasticity for a phase-field regularisation of brittle, cohesive and ductile fracture: One-dimensional examples, *International Journal of Mechanical Sciences*, doi: 10.1016/j.ijmecsci.2017.05.047, in press, 2017.

[11] R. Alessi, F. Freddi, Phase-field modelling of failure in hybrid laminates. *Composite Structures*, Vol. **181**, pp. 9–25, 2017.

[12] K. Pham, J.-J. Marigo, and C. Maurini. The issues of the uniqueness and the stability of the homogeneous response in uniaxial tests with gradient damage models. *J. Mech. Phys. Solids*, **59**, pp. 1163–1190, 2011.

[13] M. Gurtin, and L. Anand. Thermodynamics applied to gradient theories involving the accumulated plastic strain: the theories of aifantis and fleck & hutchinson and their generalization. *J. Mech. Phys. Solids*, **57**, pp. 405–421, 2009.

[14] E. Baioni, R. Alessi, V. Corinaldesi, G. Lancioni, R. Rizzini, Feasibility Study of a Table Prototype Made of High-Performance Fiber-Reinforced Concrete. *Technologies*, Vol. **5**(41), pp. 1–13, 2017.